

# Model-Agnostic Population Inference for Gravitational-Wave Astronomy: From LIGO to LISA

Yi-kun Li, Cheng Cheng, and Lang Cui\*

*State Key Laboratory of Radio Astronomy and Technology,  
Xinjiang Astronomical Observatory, CAS, 150 Science 1-Street, Urumqi 830011, China and  
School of Astronomy and Space Science, University of Chinese  
Academy of Sciences, No.19A Yuquan Road, Beijing, 100049, China*

Yun Fang\*

*Institute of Fundamental Physics and Quantum Technology, Ningbo University, Ningbo 315211, China and  
School of Physical Science and Technology, Ningbo University, Ningbo 315211, China*

(Dated: February 3, 2026)

Characterizing the population of compact binary mergers is a primary scientific objective for current and future gravitational-wave observatories. Inferring the intrinsic distribution of these events is a challenging inverse problem, complicated by detector selection biases and measurement uncertainties. Traditional parametric inference methods are fundamentally limited by the need to presuppose a specific functional form for the astrophysical distribution. This rigid assumption can introduce model-dependent biases and become computationally intractable in high-dimensional parameter spaces. To overcome these limitations, we introduce a inference framework powered by deep generative modeling. We develop a flexible, data-driven population model using a Correlated Compound-Mixture Density Network. This architecture integrates mixture models to handle multimodality, Gaussian copulas for parameter dependencies, and a library of flexible marginal distributions. The network is trained to approximate the posterior distribution of the population's hyperparameters using amortized variational inference with Normalizing Flows on catalogs of gravitational-wave events. We demonstrate the framework's capabilities in two distinct regimes. First, using simulated catalogs of supermassive black hole binary mergers for the Laser Interferometer Space Antenna (LISA), we show that the method accurately recovers complex three-dimensional distributions and absolute merger rates from sparse datasets, effectively correcting for selection effects and measurement uncertainties. Second, we validate the framework on real observational data from the LIGO-Virgo-KAGRA GWTC-3 catalog, successfully inferring the population of stellar-mass binary black holes using an injection-based selection effect correction. Our results confirm that the method is robust, scalable, and applicable across different detector sensitivities and source populations. This framework represents a step toward scalable, data-driven methodologies capable of handling the immense data volume and complexity of next-generation observatories.

## I. INTRODUCTION

Gravitational-wave (GW) astronomy has transitioned from a theoretical prediction to a precision observational science. Since the historic first detection of a binary black hole merger [1], the field has witnessed a rapid expansion in the number of observed events. The LIGO-Virgo-KAGRA (LVK) network has now reported confident detections numbering in the hundreds [2, 3], providing a growing census of compact object binaries. These observations offer unprecedented insights into the population of compact objects, allowing us to study the astrophysical formation channels of stellar-mass black holes [4–6].

This observational landscape will be revolutionized by next-generation facilities. The space-based Laser Interferometer Space Antenna (LISA) [7] will open the millihertz frequency band, targeting supermassive black hole (SMBH) binaries and enabling the study of sources across cosmic time. It will be complemented by other space-based missions such as Taiji [8] and TianQin [9], forming

a space-based network that significantly enhances source localization and parameter precision. On the ground, third-generation (3G) experiments like the Einstein Telescope (ET) [10] and Cosmic Explorer (CE) [11] aim to detect mergers from the early universe ( $z > 10$ ), effectively mapping the entire history of stellar-mass black hole assembly.

Inferring the intrinsic astrophysical population distributions of source parameters from a catalog of noisy, biased observations is a challenging inverse problem, typically addressed within the framework of Hierarchical Bayesian Inference (HBI) [12–14]. HBI connects individual event measurements to population hyperparameters  $\Lambda$  while rigorously accounting for measurement uncertainties and selection effects [15–17]. Critical to this process is the correction for Malmquist bias—the tendency to detect intrinsically louder sources from a larger volume—which requires accurate modeling of the detector's selection function  $P_{\text{det}}(\theta)$  [13, 16, 18].

Traditionally, HBI has relied on phenomenological parametric models, such as “Power Law + Peak” for black hole masses, which assume a specific functional form for the underlying distribution [2, 19, 20]. While

\* Corresponding author: fangyun@nbu.edu.cn, cuiLang@xao.ac.cn

these models have been successful in extracting first-order features, they suffer from two principal limitations. First, they are subject to model misspecification bias; imposing a rigid functional form can mask complex substructures or introduce spurious features if the true population deviates from the model assumptions [19, 21–24]. Second, as the number of hyperparameters increases to accommodate more complex models, traditional sampling methods like Markov Chain Monte Carlo (MCMC) [25] face the “curse of dimensionality,” making inference computationally prohibitive [13, 26].

To overcome these limitations, the field is increasingly exploring semi-parametric and non-parametric approaches. Methods using cubic splines [19, 22], binned Gaussian processes [27], or Dirichlet process mixture models [28] allow the data to dictate the complexity of the population density. These flexible methods have provided independent confirmation of features like the  $35M_{\odot}$  pile-up while revealing potential tensions with standard parametric fits [23, 29]. However, they often come at a steep computational cost, particularly when calculating the selection effect normalization for high-dimensional, flexible models [16].

Machine learning (ML) and deep generative models offer a compelling solution to these computational challenges. Techniques such as Normalizing Flows (NFs) [30–34] and Neural Posterior Estimation (NPE) [35, 36] enable the construction of highly flexible, model-agnostic population representations that can be evaluated and sampled efficiently [18, 26, 37]. By learning the mapping from latent spaces to complex data distributions, these models can capture arbitrary correlations and features without prescriptive functional forms.

Building on the standard hierarchical Bayesian framework for gravitational-wave population inference with selection effects [13, 14], and motivated by recent efforts to move beyond rigid parametric fits using data-driven and non-parametric reconstructions [19, 20, 22, 27, 28], we introduce a flexible, model-agnostic population inference framework that couples a correlated compound mixture population model to amortized variational inference. Our key methodological distinction from purely flow-based population representations [18, 38] is to separate the physics-facing generative population density into an explicit mixture for multimodality and a Gaussian-copula dependence structure—enabling controlled and interpretable correlation tests in the spirit of copula-based catalog studies [39, 40]—while using a normalizing-flow variational guide to efficiently approximate the hyperposterior and scale to large catalogs. We validate the framework in two complementary regimes: high-fidelity simulated LISA SMBH-binary catalogs and real LVK GWTC-3 BBH data with injection-based selection corrections, demonstrating robust recovery of joint distributions and merger-rate normalization across detector sensitivities and data volumes.

The remainder of this paper is organized as follows. Section II outlines our general population inference

framework, details the Deep Generative Model architecture, and validates the density estimation on a controlled intrinsic population. Section III presents the application to LISA, describing the generation of high-fidelity mock catalogs and demonstrating the recovery of SMBH merger rates and distributions. Section IV applies the framework to real GWTC-3 data, inferring the population of stellar-mass binary black holes and discussing the results in the context of current astrophysical knowledge. Finally, Section V summarizes our findings and discusses future prospects. Throughout this work, we adopt a standard  $\Lambda$ CDM cosmological framework with  $H_0 = 67.4 \text{ km s}^{-1}\text{Mpc}^{-1}$  and  $\Omega_m = 0.315$  [41].

## II. METHODOLOGY

Recovering the intrinsic astrophysical distribution constitutes a hierarchical inference problem [12, 13]. Our objective is to determine the posterior distribution for a set of hyperparameters,  $\boldsymbol{\Lambda}$ , that govern the underlying population, given a collection of observed data  $\{D_i\}$ . This section presents the general mathematical framework and validates the method on a controlled intrinsic population.

### A. Population Inference Framework

An inhomogeneous Poisson process describes the detection of gravitational-wave events [14]. For a catalog containing  $N_{\text{obs}}$  events with measured data  $\{D_i\}$ , the full likelihood combines the Poisson probability of the observed event count with the joint likelihood of the event properties:

$$p(\{D_i\}, N_{\text{obs}} | \boldsymbol{\Lambda}, \mathcal{R}_{\text{yr}}) = \frac{e^{-N_{\text{exp}}} N_{\text{exp}}^{N_{\text{obs}}}}{N_{\text{obs}}!} \times \prod_{i=1}^{N_{\text{obs}}} \frac{\int p(D_i | \boldsymbol{\theta}) P_{\text{det}}(\boldsymbol{\theta}) p_{\text{pop}}(\boldsymbol{\theta} | \boldsymbol{\Lambda}) d\boldsymbol{\theta}}{\mathcal{R}_{\text{yr}} T_{\text{obs}} \alpha(\boldsymbol{\Lambda})}, \quad (1)$$

Here,  $p(\boldsymbol{\theta} | D_i)$  denotes the posterior from parameter estimation of each individual event,  $P_{\text{det}}(\boldsymbol{\theta})$  denotes the detection probability, and  $p_{\text{pop}}(\boldsymbol{\theta} | \boldsymbol{\Lambda})$  denotes the population model. The expected number of detections,  $N_{\text{exp}}$ , over an observation time  $T_{\text{obs}}$  depends on the intrinsic annual merger rate,  $\mathcal{R}_{\text{yr}}$ , and the detection efficiency  $\alpha(\boldsymbol{\Lambda})$ :

$$N_{\text{exp}} = \mathcal{R}_{\text{yr}} T_{\text{obs}} \alpha(\boldsymbol{\Lambda}), \quad \alpha(\boldsymbol{\Lambda}) = \int P_{\text{det}}(\boldsymbol{\theta}) p_{\text{pop}}(\boldsymbol{\theta} | \boldsymbol{\Lambda}) d\boldsymbol{\theta}. \quad (2)$$

The term  $\alpha(\boldsymbol{\Lambda})$  is defined as the average probability that an event drawn from the intrinsic population will be detectable.  $\alpha(\boldsymbol{\Lambda})$  depends on the shape hyperparameters  $\boldsymbol{\Lambda}$  because different population distributions place different fractions of their events in the high signal-to-noise, easily detectable regime.

A key property of this likelihood structure is that the rate and shape parameters couple through the detection efficiency. Crucially, the  $\mathcal{R}_{\text{yr}}$  term reduces after algebraic simplification, which enables a powerful inference strategy that proceeds in two stages [13, 14]. We infer the posterior  $p(\boldsymbol{\Lambda}|\{D_i\})$  for the shape hyperparameters using the marginalized likelihood:

$$p(\{D_i\}|\boldsymbol{\Lambda}) \propto \left[ \int P_{\text{det}}(\boldsymbol{\theta}) p_{\text{pop}}(\boldsymbol{\theta}|\boldsymbol{\Lambda}) d\boldsymbol{\theta} \right]^{-N_{\text{obs}}} \times \prod_{i=1}^{N_{\text{obs}}} \int p(\boldsymbol{\theta}|D_i) P_{\text{det}}(\boldsymbol{\theta}) p_{\text{pop}}(\boldsymbol{\theta}|\boldsymbol{\Lambda}) d\boldsymbol{\theta}. \quad (3)$$

We evaluate the numerator integrals via Monte Carlo averaging over posterior samples and the denominator via Monte Carlo integration over the population model; the latter step corrects for selection bias.

Given the posterior for  $\boldsymbol{\Lambda}$ , we then infer the merger rate  $\mathcal{R}_{\text{yr}}$  using the Poisson term. The posterior for the rate, conditional on the observed event counting, is

$$p(\mathcal{R}_{\text{yr}}|N_{\text{obs}}, \boldsymbol{\Lambda}) \propto p(\mathcal{R}_{\text{yr}}) \frac{e^{-\mathcal{R}_{\text{yr}} T_{\text{obs}} \alpha(\boldsymbol{\Lambda})} (\mathcal{R}_{\text{yr}} T_{\text{obs}} \alpha(\boldsymbol{\Lambda}))^{N_{\text{obs}}}}{N_{\text{obs}}!}, \quad (4)$$

where  $p(\mathcal{R}_{\text{yr}})$  is the prior on the rate. For an uninformative prior, this conjugate structure reduces to a Gamma distribution [42], making rapid analytical inference tractable.

This inference strategy offers a methodological advantage: it decouples the computationally intensive shape inference, which requires training the neural network, from the straightforward rate inference, which can be performed analytically or with simple sampling. The resulting framework ensures that the inferred intrinsic event rate properly accounts for selection effects through the  $\alpha(\boldsymbol{\Lambda})$  term, which is automatically computed from the learned population model. Together, the shape inference determines the detection efficiency, which in turn governs the rate inference, forming a complete, self-consistent framework for inferring both the distribution and the absolute merger rate.

## B. Correlated Compound Mixture Density Network

Astrophysical merger distributions are expected to exhibit significant complexity. Multimodality may arise from distinct formation channels, while parameter correlations are commonly observed in gravitational-wave populations [26, 27]. To capture these features without imposing rigid functional forms, we construct a highly flexible population model,  $p_{\text{pop}}(\boldsymbol{\theta}|\boldsymbol{\Lambda})$ , implemented as a Bayesian Neural Network (BNN), that learns directly from the data. Integrating deep generative models replaces the rigid parametric population model with a

form-agnostic approach [18]. Rather than forcing the population distribution into a predefined shape, the network approximates the distribution directly from the data, enabling the discovery of complex, multimodal, and nonlinear structures [18, 27].

The first building block of our architecture is a finite mixture of  $K$  distinct components, enabling the model to capture multimodal features that may correspond to different astrophysical formation channels [43]:

$$p(\boldsymbol{\theta}|\boldsymbol{\Lambda}) = \sum_{k=1}^K w_k p_k(\boldsymbol{\theta}|\boldsymbol{\lambda}_k). \quad (5)$$

Here,  $\{w_k\}$  denote the mixture weights satisfying  $\sum_{k=1}^K w_k = 1$ . This mixture model approximates the unknown astrophysical distribution as a weighted sum of simpler probability densities, providing a flexible basis for representing complex shapes. Empirical tests reveal that increasing the number of mixture components  $K$  generally enhances estimation fidelity without exhibiting overfitting. Beyond a certain threshold, however, further increases in  $K$  produce diminishing returns in statistical performance. We select  $K$  based on the complexity of the specific inference task, balancing model expressiveness with computational efficiency, as detailed in Sec. II D, III C, and IV B for the respective configurations.

The second building block addresses the modeling of correlations between parameters. We achieve this using a Gaussian copula [44], which separates the modeling of the marginal distributions from the dependency structure. Gaussian copulas capture elliptical correlation structures commonly observed in GW parameter dependencies [26, 27] and provide tractable likelihood evaluation [45]. Separating the marginals from the dependencies allows for controlled tests of correlation without confounding changes in the marginal distribution shapes. The joint probability density function for each mixture component is given by Sklar's theorem [46]:

$$p_k(\theta_1, \dots, \theta_D|\boldsymbol{\lambda}_k) = c_k(F_{k,1}(\theta_1), \dots, F_{k,D}(\theta_D)) \prod_{d=1}^D f_{k,d}(\theta_d). \quad (6)$$

Here,  $f_{k,d}$  and  $F_{k,d}$  denote the marginal probability density and cumulative distribution functions respectively, and  $c_k$  denotes the Gaussian copula density defined by a correlation matrix  $\boldsymbol{R}_k$ . To ensure positive definiteness during optimization, we parameterize  $\boldsymbol{R}_k$  via its Cholesky decomposition. From a methodological standpoint, the separation of marginals and dependencies is essential because it enables controlled tests of correlation independently of changes in the shapes of the marginal distributions. This approach has been proven instrumentally in discovering correlations in existing GW catalogs, such as the anticorrelation between mass ratio and effective spin in binary black holes [26, 27, 39, 40].

To accommodate a wide variety of potential shapes for the marginal distributions,  $f_{k,d}$ , our framework includes

a library of flexible functional forms. The library includes the Kumaraswamy, Truncated Pareto, and Truncated Normal distributions [47]. The complete set of learnable hyperparameters  $\Lambda$  consists of the mixture weights and the parameters governing the marginals and copulas for all  $K$  components.

We term this architecture the Correlated Compound Mixture Density Network. This compound design ensures analytical tractability of the selection function integral while providing the flexibility to capture arbitrary joint distributions without prescriptive functional forms.

### C. Amortized Variational Inference with NFs

Directly sampling the posterior distribution  $p(\Lambda|D_i)$  presents a significant challenge because standard techniques such as MCMC become computationally intractable in high dimensions. To overcome this limitation, we adopt Stochastic Variational Inference (SVI) [48], which reframes the inference task as an optimization problem. Our objective is to determine a parametric distribution  $q_\phi(\Lambda)$ , termed the variational guide, that approximates the true posterior by maximizing the Evidence Lower Bound (ELBO) [49]:

$$\mathcal{L}(\phi) = \mathbb{E}_{q_\phi(\Lambda)} [\log p(\{D_i\}, \Lambda) - \log q_\phi(\Lambda)]. \quad (7)$$

Maximizing this bound minimizes the Kullback-Leibler divergence between the approximation and the true posterior probability density.

The fidelity of this approximation depends critically on the flexibility of the variational guide  $q_\phi$ . Simple parametric families often fail to capture the complex structure of the posterior. We therefore employ an NF [31], to construct a highly expressive guide. These models transform a simple base distribution such as a standard Gaussian into a complex target density through a sequence of differentiable and invertible mappings. Our implementation utilizes affine coupling layers [50] to enable flexible transformations while maintaining a Jacobian determinant that is computationally efficient to evaluate. Figure 1 depicts the architecture schematically, and Algorithm 1 details the inference procedure.

---

### Algorithm 1 Flow-Guided Bayesian Population Inference

---

**Require:** PE samples  $\{\theta_i^{(s)}\}_{i,s}$ , PE priors  $\pi_i^{(s)}$ , detection model  $P_{\text{det}}$ , observation time  $T_{\text{obs}}$   
**Ensure:** Converged variational posterior  $q_\phi(\Lambda)$ , marginalized rate posterior  $p(\mathcal{R}_{\text{yr}}|\text{data})$

**Phase 1: Shape Inference via SVI**

- 1: Initialize flow parameters  $\phi$
- 2: **while** ELBO not converged **do**
- 3:     Sample  $\Lambda \sim q_\phi(\cdot)$   $\triangleright$  Reparameterization trick
- 4:     Evaluate population model  $p_{\text{pop}}(\cdot|\Lambda)$   $\triangleright$  Sec. II B
- 5:     **for**  $i = 1$  to  $N_{\text{obs}}$  **do**
- 6:          $\mathcal{L}_i \leftarrow \frac{1}{N_{\text{post}}} \sum_s \frac{P_{\text{det}}(\theta_i^{(s)}) \cdot p_{\text{pop}}(\theta_i^{(s)}|\Lambda)}{\pi_i^{(s)}} \triangleright$  Reweighting
- 7:     **end for**
- 8:      $\alpha(\Lambda) \leftarrow \int P_{\text{det}}(\theta) p_{\text{pop}}(\theta|\Lambda) d\theta \triangleright$  Eq. (2)
- 9:      $\log \mathcal{L} \leftarrow \sum_i \ln \mathcal{L}_i - N_{\text{obs}} \ln \alpha(\Lambda) \triangleright$  Eq. (3)
- 10:     ELBO  $\leftarrow \log \mathcal{L} + \ln p(\Lambda) - \ln q_\phi(\Lambda)$
- 11:      $\phi \leftarrow \text{Adam}(\nabla_\phi \text{ELBO})$
- 12: **end while**

**Phase 2: Rate Inference**

- 13: **for**  $m = 1$  to  $M$  **do**  $\triangleright M$ : number of posterior samples
- 14:     Sample  $\Lambda^{(m)} \sim q_\phi(\cdot)$
- 15:     Compute  $\alpha^{(m)} \leftarrow \alpha(\Lambda^{(m)})$
- 16:      $p^{(m)} \leftarrow \text{Gamma}(N_{\text{obs}} + 1, T_{\text{obs}} \alpha^{(m)}) \triangleright$  Eq. (4)
- 17: **end for**
- 18: **return**  $p(\mathcal{R}_{\text{yr}}|\text{data}) \approx \frac{1}{M} \sum_m p^{(m)}(\mathcal{R}_{\text{yr}})$

---

A distinct advantage of combining SVI with NFs is the capability for amortized inference [35, 37]. Once trained, the network generates posterior samples rapidly for any new dataset without requiring repeated sampling chains. This efficiency reduces the computational cost by several orders of magnitude and makes it feasible to analyze large catalogs or explore extensive model spaces that would otherwise remain inaccessible [18, 38].

We implemented the framework using PyTorch [51] and Pyro [52]. The variational guide consists of 8 affine coupling layers. Each transformation is parameterized by a multilayer perceptron containing 128 hidden units with ReLU activations. We optimized the model parameters using the Adam algorithm with an initial learning rate of  $10^{-3}$  and a cosine annealing scheduler. Training proceeded for 1000 epochs following a 500 period warmup phase. We monitored convergence using the ELBO calculated on a validation set comprising 10 percent of the data.

### D. Validation of Core Density Estimation

We first validate the core density estimation capability of our network in a simplified toy model, excluding selection effects and measurement uncertainty. For this validation, we employed a mixture model with  $K = 6$  components, comprising 2 Kumaraswamy, 2 Truncated Pareto, and 2 Truncated Normal distributions, to capture the fine-grained details of the event distribution. We trained the network directly on 500 true intrinsic events

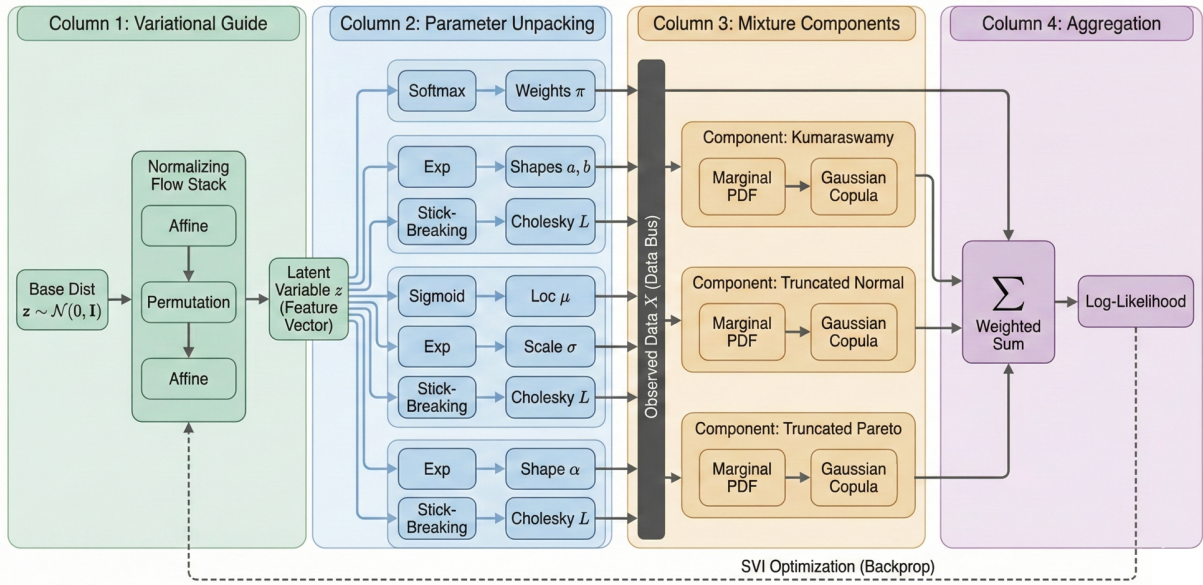


Figure 1: Technical Architecture of the Flow-Guided Correlated Compound Mixture Density Network. The network processes the latent variable  $z$  (Column 1) via an NF, unpacking it (Column 2) into parameters for specific mixture components (Column 3: Kumaraswamy, Truncated Normal, Truncated Pareto). The vertical “Data Bus” emphasizes that the observed data  $X$  feeds directly into the physics-based mixture components. Finally, these components are aggregated (Column 4) to compute the log-likelihood. Note the clear separation between the neural variational guide (green) and the physics-based mixture model (orange).

to test whether the network could accurately learn and reproduce a known, complex three-dimensional distribution from a sparse dataset.

We compared 10,000 samples from the learned distribution to the ground-truth catalog using a suite of statistical tests. We chose this large sample size, with  $N = 10,000$ , to minimize sampling noise in the generated distribution, thereby enabling a rigorous assessment of the network’s learned probability density function against the underlying structure of the training data. Kolmogorov-Smirnov (KS) tests on the marginal distributions yielded p-values of 0.274 for  $\log_{10} M_\bullet$ , 0.517 for  $z$ , and 0.259 for  $q$ , all above the standard significance threshold of 0.05. A nonparametric energy distance hypothesis test on the full three-dimensional joint distribution [53] yielded a p-value of 0.275, providing strong evidence that the learned joint distribution is statistically consistent with the ground truth. Figure 2 confirms this agreement.

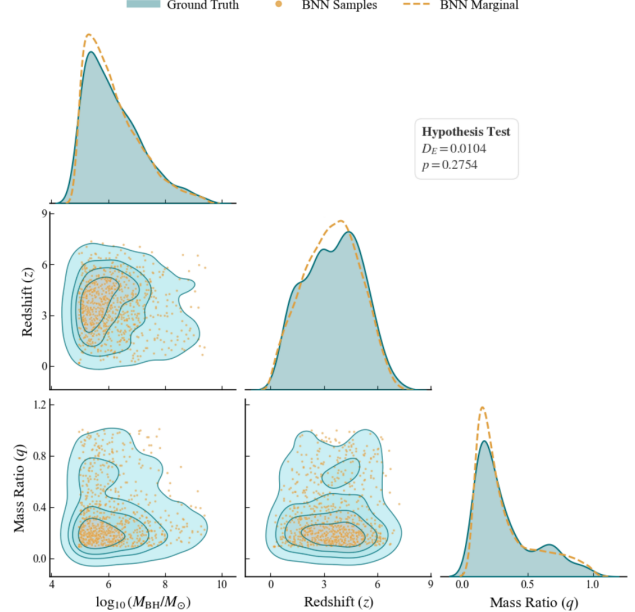


Figure 2: Validation of the density estimation network on the toy model (no selection effects). The corner plot compares the true intrinsic population (orange dashed lines/points) with the distribution learned by the network (blue contours/shaded regions).

### III. APPLICATION TO LISA: SUPERMASSIVE BLACK HOLE BINARIES

The future LISA mission will offer a unique insight into the population of SMBH binary mergers across cosmic time. This section details the generation of realistic SMBH binary catalogs and demonstrates the ability of our framework to accurately recover intrinsic distributions and merger rates.

#### A. Construction of the Intrinsic Population

To evaluate the performance of our inference framework, we first establish a physically motivated ground-truth population. Our intrinsic population model combines several key astrophysical ingredients to derive the comoving differential SMBH merger rate density,  $\mathcal{R}(M_\bullet, q, z)$ . We begin with the galaxy stellar mass function, which describes the number density of host galaxies [54, 55], and convolve it with an empirical galaxy merger rate calibrated against cosmological simulations [56–59]. Galaxies are connected to their central SMBHs via a scattered linear relation between the logarithmic black hole and stellar masses [60–63]. Recently, similar analytical toy models have been explored to benchmark inference codes [64].

By marginalizing over all host galaxy properties, we obtain the intrinsic rate density. The final differential event rate in the observer’s frame is then given by:

$$\frac{d^3 N_{\text{int}}}{d \log_{10} M_\bullet dq dz} = \mathcal{R}(M_\bullet, q, z) \frac{dV_c}{dz} \frac{1}{1+z}, \quad (8)$$

where  $V_c$  is the comoving volume element. For a detailed list of all astrophysical parameters used, see Appendix A. The population model is defined over a three-dimensional parameter space: black hole mass  $M_\bullet \in [10^5, 10^{10}] M_\odot$ , or equivalently  $\log_{10}(M_\bullet/M_\odot) \in [5, 10]$ ; redshift  $z \in [0.21, 7.5]$ ; and mass ratio  $q \in [0.1, 1.0]$ . Integration of this rate density over a 4-year observation period yields an expected number of intrinsic events  $N_{\text{int}} \approx 14$  and detectable events  $N_{\text{obs}} \approx 13$ .

#### B. Simulation of the Observation Process

For each intrinsic event, we model its observation by LISA. We employ the **IMRPhenomA** waveform model in the frequency domain to describe the GW signal from spinless binaries [65, 66]. Neglecting spin in this paper is to focus on the validation of the inference framework itself without loss of generality regarding the method’s efficiency. We quantify the detectability of each signal by its network signal-to-noise ratio,  $\rho$ , calculated using the LISA noise power spectral density [67], with instrumental noise and confusion noise from unresolved Galactic binaries [68].

Detection is a probabilistic process which will introduce selection bias. We model this bias with a smooth sigmoid function for the detection probability,  $P_{\text{det}}(\rho)$ , centered on a nominal SNR threshold of  $\rho_{\text{th}} = 8$  [69] with a characteristic transition width of  $\Delta\rho = 1.0$ . We classify an intrinsic event as detectable based on a random draw weighted by this probability. To enable efficient gradient optimization during training, we employ a fast, differentiable surrogate model for the SNR calculation [70]. Implemented as a multi-layer perceptron (MLP) trained on precomputed SNR values, this surrogate accelerates the Monte Carlo integration of the selection function by several orders of magnitude compared to direct waveform computation.

For each detected event, we simulate measurement uncertainty using the Fisher Information Matrix formalism [71, 72]. In the limit of high SNR, the posterior distribution over the parameters  $\boldsymbol{\theta} = \{\log_{10} M_\bullet, z, q\}$  is well approximated by a multivariate Gaussian distribution,  $\mathcal{N}(\boldsymbol{\theta}_{\text{true}}, \boldsymbol{\Gamma}^{-1})$ , where  $\boldsymbol{\Gamma}$  is the Fisher matrix. We draw posterior samples from this distribution for each event to emulate the outputs of a parameter estimation pipeline. This Gaussian approximation is sufficiently accurate for our population-level validation, particularly given our smooth selection function which naturally favors higher SNR events where the Fisher approximation is reliable.

To validate the robustness of the framework across realistic LISA mission scenarios, we generated mock catalogs at multiple scales. Intrinsic populations of  $N_{\text{int}} \in \{20, 50, 200, 500\}$  events yield observed catalogs of 17, 42, 166, and 412 events, respectively, after applying the selection function. The smallest catalog sizes,  $N_{\text{int}} = 20$  and 50, are consistent with conservative LISA detection forecasts over a 4-year mission [69], while the larger catalogs test performance in optimistic scenarios or extended mission durations. Figure 3 presents the projected distributions for a representative catalog with  $N_{\text{int}} = 50$  yielding  $N_{\text{obs}} = 42$ , visualizing the intrinsic population and the detectable events, highlighting the selection bias and measurement uncertainties. The SNR values of these simulated events range from tens to tens of thousands. Extreme parameters, specifically low  $q$  or high  $\log_{10} M_\bullet$ , yield lower SNR values and distinct error bars, whereas error bars are negligible for events with high SNR.

#### C. Recovering the Intrinsic Distribution

Having generated the mock observations, we now apply our framework to recover the intrinsic population properties. The primary challenge is to accurately reconstruct the three-dimensional joint distribution over mass, redshift, and mass ratio, along with the absolute merger rate, from the biased observed catalogs. This capability is a crucial step for full global analysis pipelines [73, 74]. To validate the robustness of the framework across the range of catalog sizes anticipated for actual LISA observations, we tested it on catalogs of

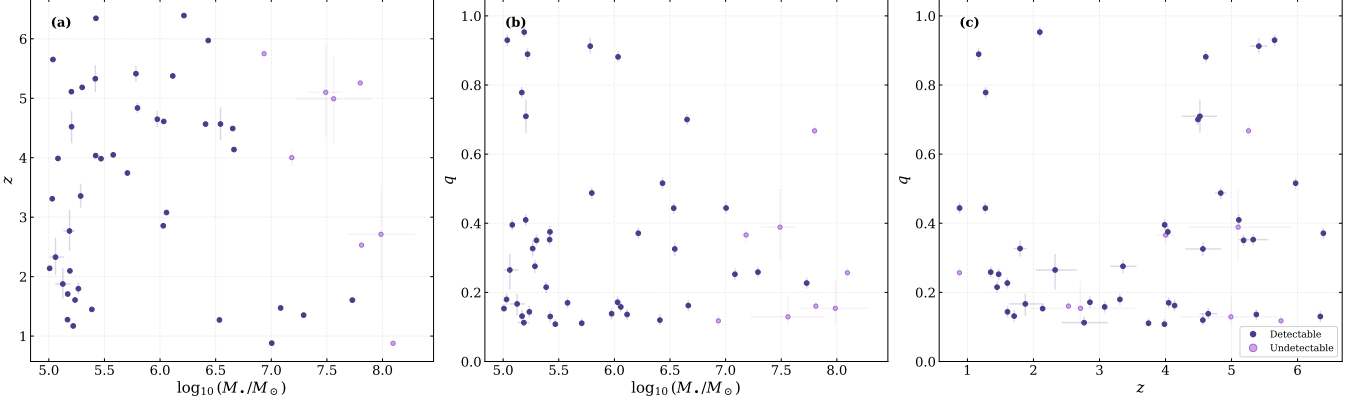


Figure 3: Projected distributions of the intrinsic ( $N_{\text{int}} = 50$ ) and detectable ( $N_{\text{obs}} = 42$ ) supermassive black hole binary merger populations in the LISA parameter space. The detectable events (dark slate blue) are distinguished from the undetectable events (plum). (a) Primary mass versus redshift. (b) Primary mass versus mass ratio. (c) Redshift versus mass ratio. Error bars represent 90% credible intervals derived from the Fisher Information Matrix.

$N_{\text{int}} \in \{20, 50, 200, 500\}$  intrinsic events, corresponding to  $N_{\text{obs}} \in \{17, 42, 166, 412\}$  observed events after selection. These scenarios span from conservative forecasts for a 4-year mission [69] to optimistic or extended mission yields.

For these analyses, we utilized a streamlined model with  $K = 2$  components, consisting exclusively of Kumaraswamy distributions. For the Monte Carlo integration of the selection function in Eq. 3, we used  $N_{\text{MC}} = 10,000$  to 40,000 samples to ensure stability, and approximated the integrals over single event posteriors using  $N_{\text{post}} = 1000$  samples drawn from the Fisher approximation.

Table I presents a systematic comparison of statistical performance across all four catalog scales. For this quantitative assessment, we adopted a specific sampling protocol: for each catalog size  $N_{\text{int}}$ , we drew exactly  $N_{\text{int}}$  events from the distribution learned by the BNN. This protocol is crucial for a fair comparison. Since the ground truth catalog is a single realization of size  $N_{\text{int}}$  subject to Poissonian shot noise, comparing it against a smooth analytical distribution or a massive sample would incorrectly penalize the model for not capturing random fluctuations inherent to that specific realization. By matching the sample sizes, we test whether the BNN could generate a realization which is statistically indistinguishable from the true observed realization.

The results demonstrate a clear trend: the framework maintains high statistical consistency with the ground truth events even in regimes where data are sparse, such as  $N_{\text{int}} = 20$ , and progressively refines its accuracy with data volume increases. The KS test p-values for the marginal distributions remain well above the 0.05 significance threshold across all scales, and the energy distance test on the full three-dimensional joint distribution consistently indicates strong fidelity, with  $p > 0.05$ .

The p-values generally decrease as  $N$  increases; for example, the energy distance test yields  $p = 0.743$  at

Table I: Statistical consistency metrics across realistic LISA catalog sizes. P-values from KS tests on one-dimensional marginals and energy distance tests on the three-dimensional joint distribution. All p-values  $> 0.05$  indicate failure to reject the null hypothesis that the learned distribution matches the ground truth.

$N_{\text{int}}$	$N_{\text{obs}}$	KS: $\log_{10} M_{\bullet}$	KS: $z$	KS: $q$	3D	Energy Dist.
20	17	0.832	0.983	0.571	<b>0.743</b>	
50	42	0.549	0.396	0.272	<b>0.788</b>	
200	166	0.142	0.713	0.628	<b>0.607</b>	
500	412	0.111	0.613	0.666	<b>0.204</b>	

$N = 20$  compared to  $p = 0.204$  at  $N = 500$ . This behavior shows the increasing statistical power of the tests: as the sample size grows, the tests become more sensitive to discrepancies between the learned and true distributions. At a low value  $N$ , the large sampling noise masks small bias, resulting in high p-values. At a high value  $N$ , the sample is large enough to detect subtle deviations. Crucially, even at  $N = 500$ , where the test is most sensitive, the p-values remain above the rejection threshold. This result confirms that the approximation error of the BNN is statistically negligible relative to the intrinsic scatter of the data.

The visual comparison in Fig. 4 corroborates these quantitative findings across all catalog sizes. These visualizations visually corroborate that our architecture is capable of performing high-quality population inference on biased and noisy data across varying data scales.

The strong performance at  $N_{\text{int}} = 20$  indicates that the framework can constrain scientifically meaningful population effectively even under pessimistic detection scenarios or in the early phases of the LISA mission. The monotonic improvement with catalog size suggests that the method will scale to leverage larger datasets as they be-

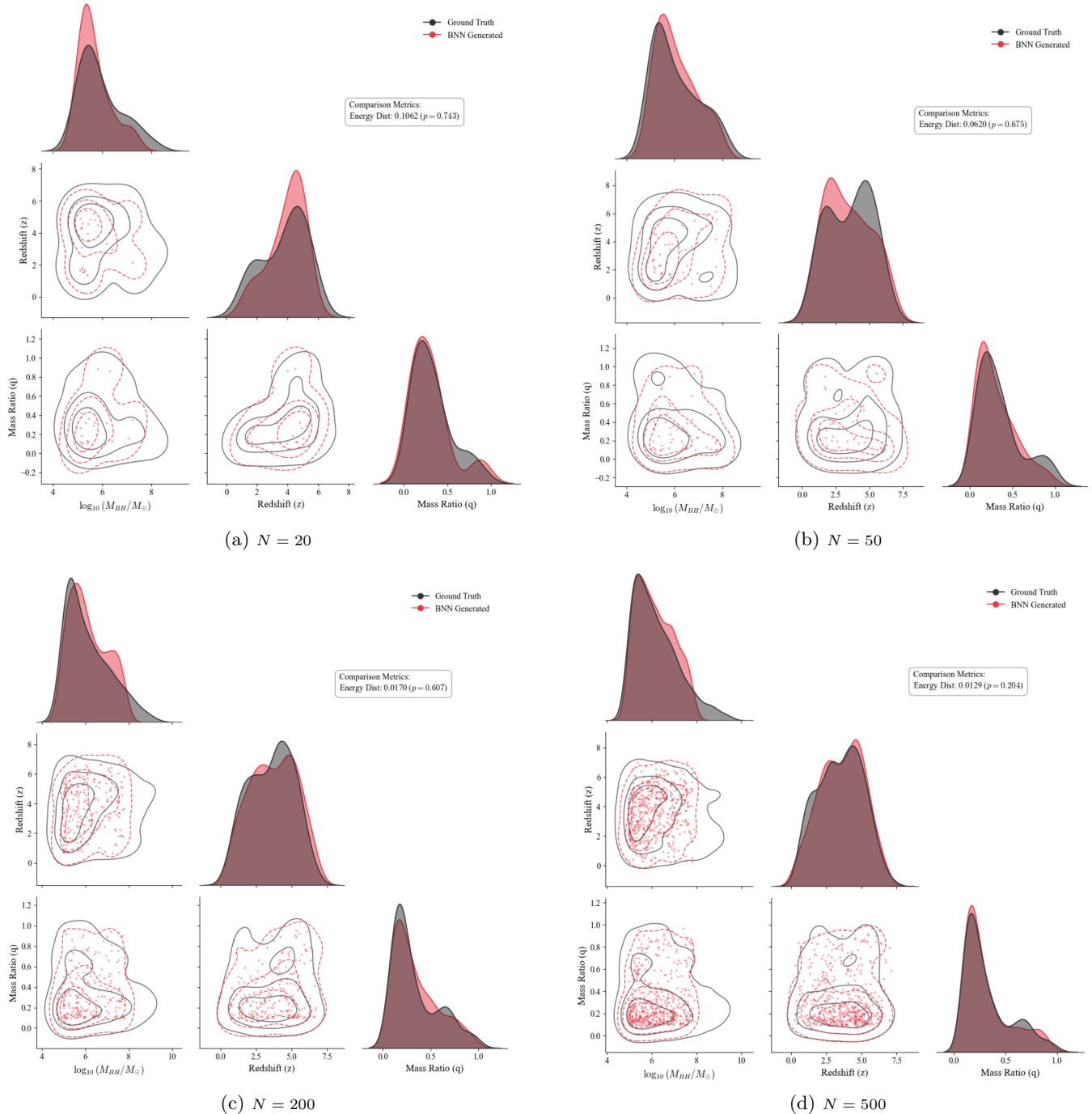


Figure 4: Scalability validation across LISA catalog sizes ( $N_{\text{int}} \in \{20, 50, 200, 500\}$ ). Comparison between True Intrinsic distribution and BNN Reconstruction. The contours progressively refine as data volume increases, demonstrating data-adaptive capability.

come available, without requiring fundamental methodological adjustments. This adaptive behavior contrasts with traditional parametric HBI, where model complexity must be carefully balanced against sample size to avoid overfitting or underfitting.

Beyond recovering the shape of the intrinsic distribution, as validated in Fig. 4, a complete astrophys-

ical characterization requires determining the absolute merger rate. Figure 5 presents the validation of our event count inference across all four catalog sizes. This validation assesses the model's consistency in two complementary regimes. First, we verify the intrinsic parameter recovery by inferring the total intrinsic number of events,  $N_{\text{int}}$ , which is directly proportional to the merger rate

$\mathcal{R}_{\text{yr}}$  through the detection efficiency  $\alpha(\Lambda)$ . Second, we perform an observable consistency check by predicting the expected number of observed events,  $N_{\text{obs}}$ , to ensure the model is consistent with the actual data fed into it.

The results in Fig. 5 demonstrate that our framework accurately infers the intrinsic event count  $N_{\text{int}}$ , and thus the rate  $\mathcal{R}_{\text{yr}}$ , across all data volume regimes. In Test 1, shown in blue, the ground truth lies well within the inferred posterior distributions. Crucially, the uncertainty scales decreasingly with data size: the posterior narrows significantly as  $N$  increases from 20 to 500, which is consistent with the expected  $\sim 1/\sqrt{N}$  reduction in Poisson error.

Test 2, shown in green, confirms that our calculation of the detection efficiency  $\alpha(\Lambda)$  is accurate. The model precisely predicts the number of events that should be observed given the inferred population, matching the actual catalog size. This consistency check is an indicator that the selection effects are being properly modeled and corrected for, validating the theoretical approach outlined in Sec. II A.

#### D. Comparison with a Parametric Estimation Method

To test the performance of our framework, we conducted a direct comparison against a traditional parametric MCMC method in a simplified two-dimensional scenario with  $q = 1$  fixed. The computationally prohibitive cost of running a converged MCMC chain on the full three-dimensional problem with selection effects necessitated this restriction. For the MCMC baseline, we assumed the true functional form of the merger rate was known and inferred its four governing hyperparameters. Both experiments used mock catalogs of approximately 400 observed SMBH merger events with LISA selection effects applied; for the BNN, we employed  $K = 5$  components based on Beta distributions.

Table II presents the results when the MCMC is given the correct functional form (Eq. 8). As expected, the parametric method achieves near-perfect reconstruction (Jensen-Shannon (JS) divergence of 0.03, Pearson correlation of 0.99). Our network, operating without any knowledge of the underlying model, robustly learns the distribution with a Pearson correlation of 0.94—demonstrating that a data-driven approach can provide a high-accuracy reconstruction without requiring strong prior assumptions.

When the underlying physics deviates from the assumed parametric form, the non-parametric approach is much more robust. To test this, we generated a mock catalog from an alternative “Bimodal Mass + Cosmic Noon Peak” model featuring two key properties: first, a bimodal mass distribution with Gaussian peaks at  $\log_{10}(M_{\bullet}/M_{\odot}) = 5.5$  and 7.5, representing distinct light seed and heavy seed formation channels; and second, redshift evolution that is not monotonic but instead peaks

Table II: Quantitative comparison when the MCMC model is *correctly specified*. The MCMC, given exact knowledge of the underlying functional form, achieves near-perfect reconstruction.

Comparison	JS Divergence	Pearson Corr.
BNN vs Truth	0.0926	0.9395
MCMC vs Truth	0.0293	0.9948
BNN vs MCMC	0.0905	0.9433

Table III: Quantitative comparison when the MCMC model is *misspecified*. The BNN significantly outperforms the rigid parametric model.

Comparison	JS Divergence	Pearson Corr.
BNN vs Truth	0.1095	0.9537
MCMC vs Truth	0.2211	0.8397
BNN vs MCMC	0.2331	0.8442

at  $z \approx 2.5$  with a subsequent decline. Both features are structurally incompatible with the smooth power law forms assumed by the MCMC.

Table III shows a reversal: the BNN achieves a JS divergence approximately half that of the MCMC, specifically 0.11 versus 0.22, capturing the bimodal mass structure and the redshift evolution that the rigid parametric model cannot represent. These results indicate an inevitable possibility: when the true underlying astrophysics is unknown, relying on parametric models risks introducing systematic biases. The computational efficiency of our framework, which requires training in minutes compared to hours of surrogate construction for MCMC as illustrated in Figure 6, provides both flexibility and scalability for future GW surveys.

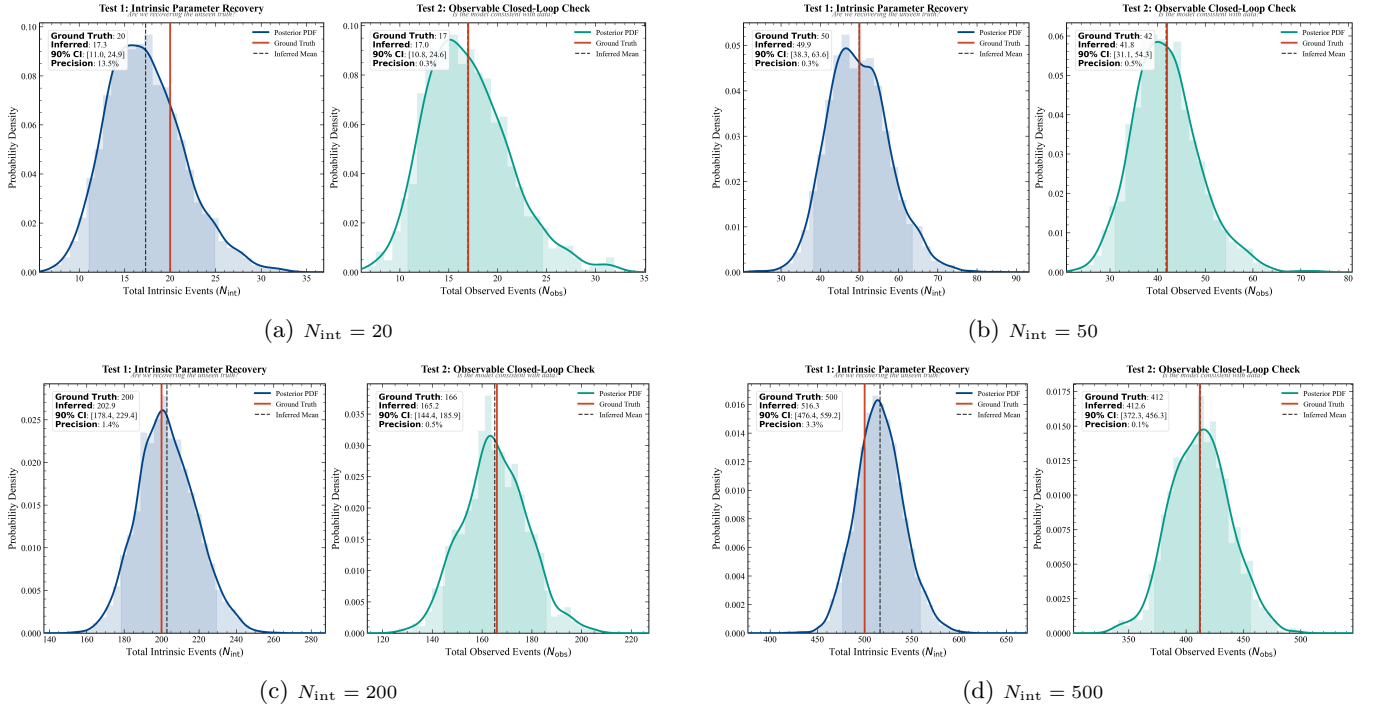


Figure 5: Validation of event count inference. Each panel shows posteriors for intrinsic count  $N_{\text{int}}$  (blue) and expected observed count  $N_{\text{obs}}$  (green), compared to ground truths (red lines). The framework accurately recovers intrinsic counts across all catalog sizes.

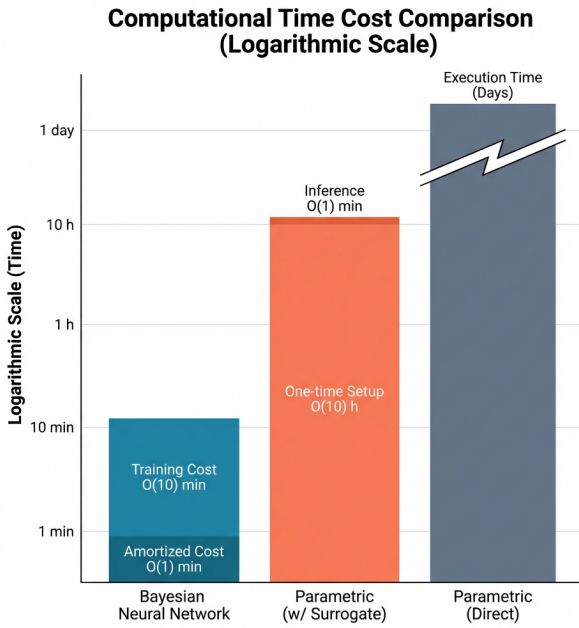


Figure 6: Computational cost comparison. Left: Neural network approach ( $\sim 10$  min training, negligible inference). Center: Surrogate-based MCMC ( $\sim 10$  hours setup,  $\sim 1$  min inference). Right: Direct parametric MCMC (days).

#### IV. APPLICATION TO LIGO: STELLAR-MASS BINARY BLACK HOLES

While the LISA analysis confirmed the framework's theoretical accuracy against a known ground truth, applying it to real observational data is still full of challenges, which include complex noise properties and non-analytical selection functions. In this section, we validate the framework on the stellar-mass binary black hole (BBH) population detected by the LIGO-Virgo-KAGRA (LVK) collaboration during the O1, O2, and O3 observing runs [2].

##### A. Data and Selection Effects

We use data from the third Gravitational-Wave Transient Catalog (GWTC-3) [2], which contains 90 confident compact binary coalescence detections. After applying physically motivated cuts to ensure robust BBH classification ( $m_2 \geq 3 M_{\odot}$  to exclude neutron stars and  $q \geq 0.2$  to avoid regions of unreliable detection efficiency), we retain 69 events for population inference. For each event, we utilize 5000 posterior samples in the source-frame parameters: primary mass  $m_1$ , redshift  $z$ , and mass ratio  $q = m_2/m_1$ . All posterior samples include associated prior weights from the original parameter estimation, enabling proper reweighting to arbitrary population models. The population model is defined over a

three-dimensional parameter space: primary mass  $m_1 \in [3, 300] M_\odot$  (equivalently,  $\log_{10}(m_1/M_\odot) \in [0.48, 2.48]$ ), redshift  $z \in [0, 3]$ , and mass ratio  $q \in [0.05, 1.0]$ . Figure 7 presents an overview of the observed BBH events, illustrating the distribution in the  $m_1$ – $z$ ,  $m_1$ – $q$ , and  $z$ – $q$  planes.

Unlike the analytical SNR approximation used for LISA, the detection efficiency for ground-based detectors must be characterized empirically through extensive injection campaigns considering the complex, time-varying noise and pipeline-specific triggers. We use the official O1+O2+O3 injection file (LIGO-T2100377-v2), which contains approximately 73 million simulated signals spanning the detection parameter space, with a complete information about which injections were successfully recovered by the search pipelines. After applying the same physical cuts as for the observed events, approximately 39,000 detected injections remain for selection effect estimation. The detection efficiency is computed empirically with importance sampling over the recovered injections:

$$\alpha(\boldsymbol{\Lambda}) = \frac{1}{N_{\text{draw}}} \sum_{j \in \text{det}} \frac{p_{\text{pop}}(\boldsymbol{\theta}_j | \boldsymbol{\Lambda})}{p_{\text{draw}}(\boldsymbol{\theta}_j)}, \quad (9)$$

where the sum runs over detected injections,  $p_{\text{draw}}$  is the injection sampling distribution, and  $N_{\text{draw}}$  is the total number of injections. This approach directly incorporates the complex, pipeline-dependent selection function without requiring analytical approximations.

## B. Inference Methodology

When working with real posterior samples from parameter estimation, the population likelihood (Eq. 3) requires careful treatment of the prior used in the original analysis. Each posterior sample must be divided by its associated prior to recover the likelihood contribution, then reweighted to the population model:

$$w_i \propto \frac{p_{\text{pop}}(\boldsymbol{\theta}_i | \boldsymbol{\Lambda})}{\pi(\boldsymbol{\theta}_i)}, \quad (10)$$

where  $\pi(\boldsymbol{\theta}_i)$  is the prior used in parameter estimation. This reweighting ensures that the inferred population is independent of the arbitrary prior choices made during individual event analyses.

Population inference with real observational data presents unique challenges due to the limited sample size and the high-dimensional nature of the importance sampling integrals. To ensure robust convergence, we introduce two stabilization mechanisms in the loss function. First, we monitor the effective sample size ( $N_{\text{eff}}$ ) of the importance weights used for the selection function integral. When  $N_{\text{eff}}$  drops below a critical threshold (set to  $4 \times N_{\text{obs}}$ ), the Monte Carlo approximation becomes unreliable, and the model risks collapsing into regions dominated by a single injection sample. This dynamic

threshold ensures that, on average, each observed event is supported by at least four effective injection samples, which we found empirically to be the minimum required to prevent the Monte Carlo variance from dominating the gradient signal. We apply a large penalty to the log-probability in such cases, effectively constraining the optimization to regions of parameter space where the selection integral is well-behaved. Second, motivated by the astrophysical expectation that binary black holes preferentially form with comparable masses [75], we apply a monotonicity regularization term that penalizes negative slopes in the marginal distribution of the mass ratio  $p(q)$ . This acts as a soft, physics-informed prior that guides the model towards physically plausible solutions, particularly in the low-information regime where the sparse data provide limited constraints on the mass ratio distribution.

We employed  $K = 4$  components comprising 2 Kumaraswamy and 2 Truncated Normal distributions, balancing model flexibility with the complexity of the stellar-mass BBH population. The single-event posterior integrals in the numerator of the likelihood are approximated using  $N_{\text{post}} = 5000$  samples directly from the parameter estimation posteriors.

## C. Inferred Population Distributions

Figure 8 presents the inferred two-dimensional joint distributions of the source parameters, revealing the correlation structure of the population. Figure 9 displays the corresponding one-dimensional marginal distributions with their associated uncertainties.

The inferred distributions are qualitatively consistent with established results from parametric analyses, including the LVK population papers [2], as detailed in Fig. 9. Regarding the primary mass (Panel a), the reconstructed mass spectrum is dominated by a peak at low masses (median  $m_1 \approx 14 M_\odot$ ), with a broad plateau-like feature extending up to  $\sim 40 M_\odot$ . This structure is qualitatively consistent with the “Power Law + Peak” models often used in parametric analyses, where the plateau corresponds to the Gaussian component associated with PISN pile-up. The distribution then exhibits a steep fall-off beyond  $\sim 60 - 80 M_\odot$ , consistent with the expected PISN mass gap. In terms of mass ratio (Panel c), the distribution displays a monotonic rise towards  $q = 1$ , with a median value of  $q \approx 0.65$ . This strong preference for symmetric binaries is a robust feature, reinforced by our physics-informed monotonicity regularization. It aligns with standard formation channels where mass transfer or dynamical exchange tends to equalize component masses. Finally, for redshift (Panel b), unlike the local volume ( $z < 1$ ) where the rate is often approximated as strictly increasing, our global fit recovers a distribution that peaks around  $z \approx 1.6$  (median  $z \approx 1.63$ ). This turnover is consistent with the peak of the cosmic star formation rate (at  $z \sim 2$ ), accounting for the time delay between star formation and binary merger. The

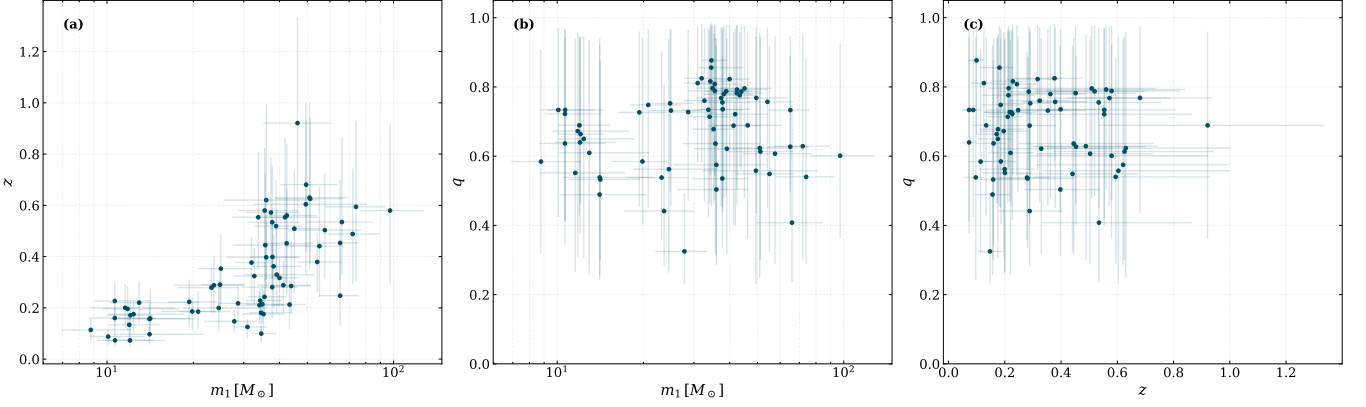


Figure 7: Overview of the 69 binary black hole events from GWTC-3 used in this analysis. The panels show the parameter distributions with 90% credible intervals (error bars) and median values (points). (a) Primary mass versus redshift. (b) Primary mass versus mass ratio. (c) Redshift versus mass ratio. The transparent error bars visualize the measurement uncertainty for each individual event.

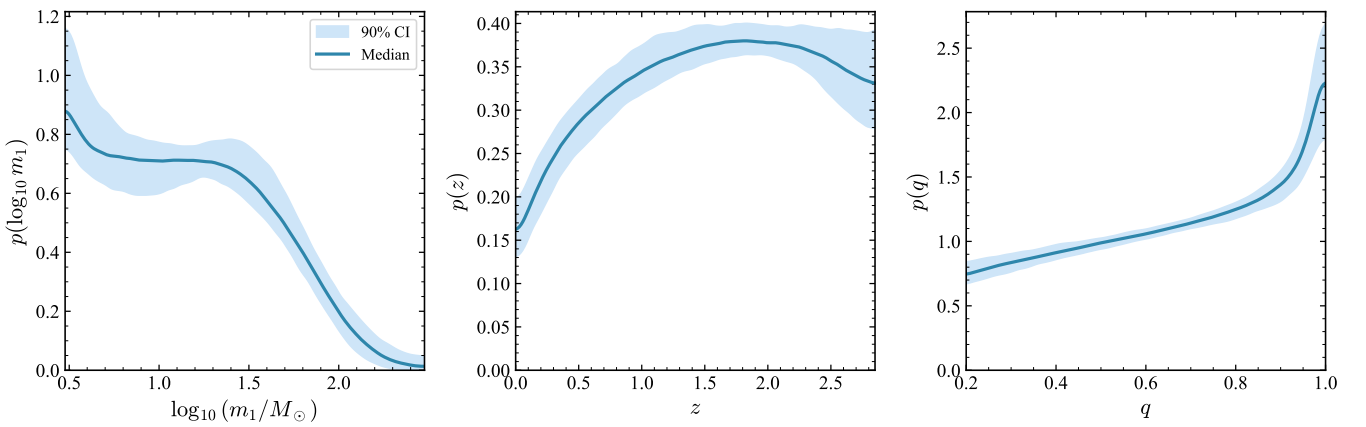
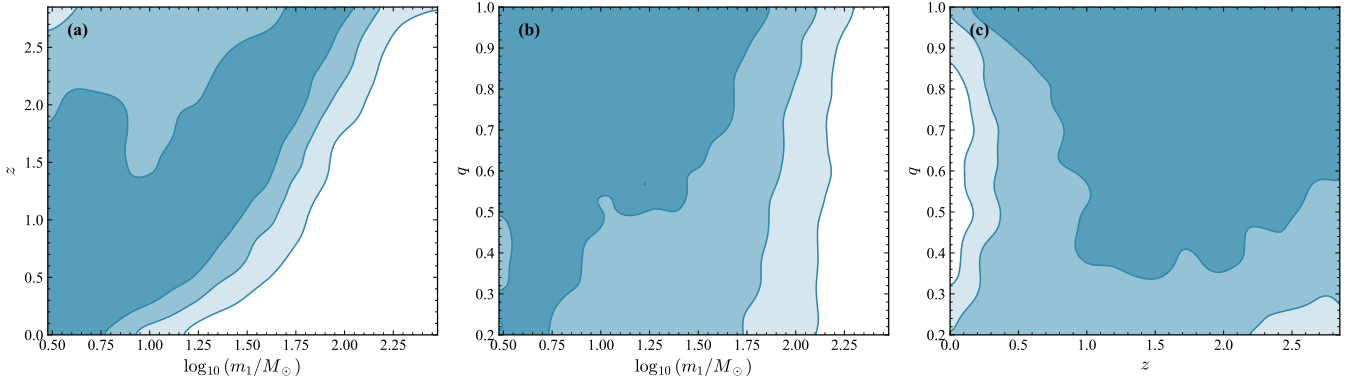


Figure 9: Reconstructed marginal distributions for LIGO BBH population. (a) Primary mass spectrum showing a peak at  $\sim 10 M_\odot$  and PISN-like fall-off. (b) Redshift evolution peaking at cosmic noon. (c) Mass ratio favoring equal-mass binaries ( $q \rightarrow 1$ ). Shaded regions represent 90% credible intervals.

broadening of the credible intervals at high  $z$  reflects the scarcity of detections near the horizon.

The ability to recover these features without assuming a specific functional form (like the Power Law + Peak model often used) validates the flexibility of our approach. This result confirms that the framework is not limited to high-SNR space-based observations but is equally effective for ground-based detectors with different noise characteristics and selection functions. We note that the credible intervals reported here represent statistical uncertainty only; systematic uncertainties from astrophysical modeling assumptions would broaden the true error budget.

## V. CONCLUSION

In this paper, we have presented a hierarchical Bayesian inference framework that combines flexible density estimation with deep generative models [18, 37]. By replacing rigid parametric models with a data-driven approach, our method addresses model-dependent bias and computational scalability challenges inherent in traditional approaches.

We have demonstrated, using both realistic mock data catalogs for LISA and real observational data from LIGO, that our framework can successfully navigate complex inverse problems. It accurately disentangles the intrinsic source distributions from strong selection biases and measurement uncertainties. For LISA, we showed that the method recovers the intrinsic three-dimensional SMBH merger distribution and absolute rate with high fidelity across a wide range of catalog sizes. For LIGO, we successfully inferred the stellar-mass BBH population from GWTC-3, validating the framework’s effectiveness on real data with injection-based selection corrections. This dual validation confirms that the method is robust, scalable, and applicable to any gravitational-wave detector, from current ground-based observatories to future space-based missions.

Our comparative analysis with a traditional MCMC method demonstrates the value of our approach. While parametric methods excel when the true model is known, our Bayesian Neural Network provides accurate reconstruction without this prior knowledge. Its computational efficiency and scalability to higher dimensions and varying data volumes make it well-suited for future astrophysical analyses. Model-agnostic inference will be particularly valuable for next-generation observatories, where the underlying physical models are not yet fully established.

Future work will focus on incorporating more sophisticated astrophysical models, including the effects of black hole spin, and applying this framework to increasingly complex datasets. The principles demonstrated here extend to other areas of GW data analysis. The emulation capability of NFs can create fast surrogates for computationally expensive population synthesis simula-

tions, bridging theoretical models of galaxy evolution and detectable GW signals [4, 18]. The computational efficiency also enables accelerated single-event parameter estimation, supporting real-time multi-messenger astronomy with rapid electromagnetic follow-up [35]. This work contributes to the development of automated inference systems capable of transforming raw detector data into scientific results with reduced human intervention [76]. By providing a flexible and scalable solution to high-dimensional inference challenges, this methodology is applicable to current and future gravitational-wave observations.

Beyond methodological advances, this framework opens new avenues for addressing fundamental astrophysical questions. For LISA, the ability to reconstruct multimodal and complex mass functions without parametric assumptions is essential for distinguishing between distinct supermassive black hole seed formation scenarios—the “Light Seed” pathway via Population III stellar remnants versus the “Heavy Seed” pathway via direct collapse [77–79]. By accurately recovering the shape of the mass function at high redshifts, including potential bimodalities or characteristic gaps, this method can provide direct observational constraints on the initial conditions of black hole growth in the early universe [80, 81]. For ground-based observations with LIGO and future third-generation detectors like the Einstein Telescope, the framework’s capacity to capture non-linear correlations in the joint parameter space enables robust discrimination between isolated binary evolution and dynamical formation channels [6, 82]. Furthermore, by resolving the mass-spin correlations characteristic of hierarchical mergers, one can identify second-generation black holes populating the pair-instability mass gap and thereby constrain the nuclear reaction rates governing massive stellar evolution [83, 84]. Looking ahead, the synergy between space-based and ground-based observatories—with LISA probing supermassive mergers at cosmic dawn and ET/CE mapping stellar-mass assembly across all redshifts—will require inference tools capable of jointly analyzing heterogeneous datasets. The flexible, scalable nature of our approach positions it as a foundational methodology for this multi-band, multi-messenger era, enabling a unified reconstruction of black hole demographics from the first seeds to the present-day population.

## ACKNOWLEDGMENTS

This work was supported by the National Key R&D Program of China (grant No. 2024YFA1611503), the Central Guidance for Local Science and Technology Development Fund (grant No. ZYYD2026JD01), and the Urumqi Nanshan Astronomy and Deep Space Exploration Observation and Research Station of Xinjiang (XJYWZ2303).

YF was supported by the National Natural Science Foundation of China (Grant No. 12405068).

## Appendix A: LISA Mock Data Generation Details

This appendix details the specific parameters and mathematical justifications for the mock data catalog described in Sec. III.

### 1. Astrophysical Model Parameters

We assume a  $\Lambda$ CDM cosmology with  $H_0 = 67.4 \text{ km s}^{-1}\text{Mpc}^{-1}$ ,  $\Omega_m = 0.315$ , and  $\Omega_\Lambda = 0.685$  [41]. The Galaxy Stellar Mass Function (GSMF) uses a double Schechter function with redshift-dependent parameters interpolated from Table IV (based on COSMOS2020 [54]).

Table IV: Discrete data points for the redshift evolution of the GSMF parameters, from [54].

$z$	$\log_{10}(M_c/M_\odot)$	$\log_{10}(\phi_1^*)$	$\alpha_1$	$\log_{10}(\phi_2^*)$	$\alpha_2$
0.35	10.93	-3.22	-1.45	-2.97	-0.66
0.65	10.98	-3.32	-1.44	-3.04	-0.79
0.95	11.01	-3.15	-1.35	-3.11	-0.72
1.30	11.01	-3.16	-1.34	-3.49	-0.56
1.75	10.88	-3.64	-1.52	-3.17	-0.55
2.25	10.80	-3.59	-1.46	-3.54	0.04
2.75	11.00	-3.66	-1.46	-9.00	0.00
3.25	10.85	-3.70	-1.46	-9.00	0.00
4.00	10.46	-3.70	-1.46	-9.00	0.00
5.00	10.33	-3.89	-1.46	-9.00	0.00
6.00	10.19	-4.30	-1.46	-9.00	0.00
7.00	10.50	-5.00	-1.46	-9.00	0.00

<sup>a</sup> Note: The units for  $\phi_{1,2}^*$  are  $\text{Mpc}^{-3}$ .

The  $M_\bullet - M_*$  relation transitions via a sigmoid at  $z = 4.0$  from a low-redshift regime ( $b = 1.17, a = -4.18, \epsilon = 0.28$  [60]) to a high-redshift regime ( $b = 1.06, a = -2.43, \epsilon = 0.69$  [62]). The galaxy merger rate follows [56].

We approximate the black hole mass ratio as the stellar mass ratio,  $q \approx \mu_*$ . Assuming the mean log-black hole mass follows  $\langle \log_{10} M_\bullet \rangle = a(z) + b(z) \log_{10} M_*$  with Gaussian scatter  $\epsilon(z)$ , the mass ratio  $q = M_{\bullet,2}/M_{\bullet,1}$  satisfies:

$$\log_{10}(q) = b(z) \log_{10}(\mu_*) + (\delta_2 - \delta_1), \quad (\text{A1})$$

where  $\delta_i$  are independent scatter terms with zero mean. Since observed slopes  $b(z)$  are of order unity [60, 62] and  $E[\delta_2 - \delta_1] = 0$ , the approximation  $q \approx \mu_*$  captures the dominant mean behavior, neglecting the intrinsic scatter  $\sigma \approx 0.3 - 0.7 \text{ dex}$ .

### 2. Observational Model Parameters

We use the LISA noise PSD from [67] with arm length  $L = 2.5 \times 10^9 \text{ m}$ , high-frequency OMS noise  $(1.5 \times 10^{-11} \text{ m})^2 \text{Hz}^{-1}$ , and acceleration noise  $(3 \times 10^{-15} \text{ ms}^{-2})^2 \text{Hz}^{-1}$ .

---

[1] B. P. Abbott *et al.* (LIGO Scientific Collaboration and Virgo Collaboration), Observation of gravitational waves from a binary black hole merger, *Phys. Rev. Lett.* **116**, 061102 (2016).

[2] R. Abbott, T. Abbott, F. Acernese, K. Ackley, C. Adams, N. Adhikari, R. Adhikari, V. Adya, C. Affeldt, D. Agarwal, *et al.*, Population of merging compact binaries inferred using gravitational waves through gwtc-3, *Physical Review X* **13**, 011048 (2023).

[3] A. Abac, I. Abouelfettouh, F. Acernese, K. Ackley, C. Adamcewicz, S. Adhikary, D. Adhikari, N. Adhikari, R. Adhikari, V. Adkins, *et al.*, Gwtc-4.0: Population properties of merging compact binaries, *arXiv preprint arXiv:2508.18083* (2025).

[4] M. Zevin, S. S. Bavera, C. P. Berry, V. Kalogera, T. Fragos, P. Marchant, C. L. Rodriguez, F. Antonini, D. E. Holz, and C. Pankow, One channel to rule them all? constraining the origins of binary black holes using multiple formation pathways, *The Astrophysical Journal* **910**, 152 (2021).

[5] S. Stevenson, C. P. Berry, and I. Mandel, Hierarchical analysis of gravitational-wave measurements of binary black hole spin-orbit misalignments, *Monthly Notices of the Royal Astronomical Society* **471**, 2801 (2017).

[6] I. Mandel and F. S. Broekgaarden, Rates of compact object coalescences, *Living Reviews in Relativity* **25**, 10.1007/s41114-021-00034-3 (2022).

[7] P. Amaro-Seoane *et al.*, Laser interferometer space antenna (2017), *arXiv:1702.00786* [astro-ph.IM].

[8] W.-R. Hu and Y.-L. Wu, The taiji program in space for gravitational wave physics and the nature of gravity, *National Science Review* **4**, 685 (2017).

[9] J. Luo, L.-S. Chen, H.-Z. Duan, Y.-G. Gong, S. Hu, J. Ji, Q. Liu, J. Mei, V. Milyukov, M. Sazhin, *et al.*, Tianqin: a space-borne gravitational wave detector, *Classical and Quantum Gravity* **33**, 035010 (2016).

[10] M. Punturo, M. Abernathy, F. Acernese, B. Allen, N. Andersson, K. Arun, F. Barone, B. Barr, M. Barsuglia, M. Beker, *et al.*, The einstein telescope: A third-generation gravitational wave observatory, *Classical and Quantum Gravity* **27**, 194002 (2010).

[11] M. Evans, R. X. Adhikari, C. Afle, S. W. Ballmer, S. Biscoveanu, S. Borhanian, D. A. Brown, Y. Chen, R. Eisenstein, A. Gruson, *et al.*, A horizon study for cosmic explorer: science, observatories, and community, *arXiv preprint arXiv:2109.09882* (2021).

[12] D. W. Hogg, J. Bovy, and D. Lang, Data analysis recipes: Fitting a model to data, arXiv preprint arXiv:1008.4686 (2010).

[13] I. Mandel, W. M. Farr, and J. R. Gair, Extracting distribution parameters from multiple uncertain observations with selection biases, *Monthly Notices of the Royal Astronomical Society* **486**, 1086 (2019).

[14] E. Thrane and C. Talbot, An introduction to bayesian inference in gravitational-wave astronomy: parameter estimation, model selection, and hierarchical models, *Publications of the Astronomical Society of Australia* **36**, e010 (2019).

[15] T. J. Loredo, Promise of bayesian inference for astrophysics, in *Statistical Challenges in Modern Astronomy*, edited by E. D. Feigelson and G. J. Babu (Springer New York, New York, NY, 1992) pp. 275–297.

[16] C. Talbot and J. Golomb, Growing pains: understanding the impact of likelihood uncertainty on hierarchical bayesian inference for gravitational-wave astronomy, *Monthly Notices of the Royal Astronomical Society* **526**, 3495 (2023).

[17] M. Mancarella and D. Gerosa, Sampling the full hierarchical population posterior distribution in gravitational-wave astronomy, *Physical Review D* **111**, 103012 (2025).

[18] K. W. Wong, G. Contardo, and S. Ho, Gravitational-wave population inference with deep flow-based generative network, *Physical Review D* **101**, 123005 (2020).

[19] N. Guttman, E. Payne, P. D. Lasky, and E. Thrane, Trends in the population of binary black holes following the fourth gravitational-wave transient catalog: a data-driven analysis, arXiv preprint arXiv:2509.09876 (2025).

[20] V. Tiwari, Exploring features in the binary black hole population, *The Astrophysical Journal* **928**, 155 (2022).

[21] C. M. Fabbri, D. Gerosa, A. Santini, M. Mould, A. Toubiana, and J. Gair, Reconstructing parametric gravitational-wave population fits from nonparametric results without refitting the data, *Physical Review D* **111**, 104053 (2025).

[22] B. Edelman, B. Farr, and Z. Doctor, Cover your basis: Comprehensive data-driven characterization of the binary black hole population, *The Astrophysical Journal* **946**, 16 (2023).

[23] A. M. Farah, B. Edelman, M. Zevin, M. Fishbach, J. M. Ezquiaga, B. Farr, and D. E. Holz, Things that might go bump in the night: Assessing structure in the binary black hole mass spectrum, *The Astrophysical Journal* **955**, 107 (2023).

[24] V. Gennari, S. Mastrogiovanni, N. Tamanini, S. Marsat, and G. Pierra, Searching for additional structure and redshift evolution in the observed binary black hole population with a parametric time-dependent mass distribution, *Physical Review D* **111**, 123046 (2025).

[25] D. Foreman-Mackey, D. W. Hogg, D. Lang, and J. Goodman, emcee: the mcmc hammer, *Publications of the Astronomical Society of the Pacific* **125**, 306 (2013).

[26] C. Talbot and E. Thrane, Measuring the binary black hole mass spectrum with an astrophysically motivated parameterization, *The Astrophysical Journal* **856**, 173 (2018).

[27] T. A. Callister and W. M. Farr, Parameter-free tour of the binary black hole population, *Physical Review X* **14**, 021005 (2024).

[28] S. Rinaldi and W. Del Pozzo, Figaro: hierarchical nonparametric inference for population studies, *Journal of Open Source Software* **9**, 6589 (2024).

[29] J. Golomb and C. Talbot, Searching for structure in the binary black hole spin distribution, *Physical Review D* **108**, 103009 (2023).

[30] D. Rezende and S. Mohamed, Variational inference with normalizing flows, in *International conference on machine learning* (PMLR, 2015) pp. 1530–1538.

[31] G. Papamakarios, E. Nalisnick, D. J. Rezende, S. Mohamed, and B. Lakshminarayanan, Normalizing flows for probabilistic modeling and inference, *Journal of Machine Learning Research* **22**, 1 (2021).

[32] D. Lanchares, O. G. Freitas, J. González-Nuevo, and J. A. Font, Assessment of normalizing flows for parameter estimation on time-frequency representations of gravitational-wave data, arXiv preprint arXiv:2505.08089 (2025).

[33] S. Colloms, C. P. Berry, J. Veitch, and M. Zevin, Exploring the evolution of gravitational-wave emitters with efficient emulation: Constraining the origins of binary black holes using normalising flows, arXiv preprint arXiv:2503.03819 (2025).

[34] D. Shih, M. Freytsis, S. R. Taylor, J. A. Dror, and N. Smyth, Fast parameter inference on pulsar timing arrays with normalizing flows, *Physical review letters* **133**, 011402 (2024).

[35] K. Leyde, S. R. Green, A. Toubiana, and J. Gair, Gravitational wave populations and cosmology with neural posterior estimation, *Physical Review D* **109**, 064056 (2024).

[36] J.-Q. Jiang, H.-L. Huang, J. He, Y.-T. Wang, and Y.-S. Piao, A fast deep-learning approach to probing primordial black hole populations in gravitational wave events, arXiv preprint arXiv:2505.15530 (2025).

[37] M. Mould, N. E. Wolfe, and S. Vitale, Rapid inference and comparison of gravitational-wave population models with neural variational posteriors, *Physical Review D* **111**, 123049 (2025).

[38] D. Ruhe, K. Wong, M. Cranmer, and P. Forré, Normalizing flows for hierarchical bayesian analysis: A gravitational wave population study, arXiv preprint arXiv:2211.09008 (2022).

[39] C. Adamcewicz and E. Thrane, Do unequal-mass binary black hole systems have larger  $\chi_{\text{eff}}$ ? probing correlations with copulas in gravitational-wave astronomy, *Monthly Notices of the Royal Astronomical Society* **517**, 3928 (2022).

[40] C. Adamcewicz, P. D. Lasky, and E. Thrane, Evidence for a correlation between binary black hole mass ratio and black hole spins, *The Astrophysical Journal* **958**, 13 (2023).

[41] N. Aghanim, Y. Akrami, M. Ashdown, J. Aumont, C. Baccigalupi, M. Ballardini, A. J. Banday, R. Barreiro, N. Bartolo, S. Basak, *et al.*, Planck 2018 results-vi. cosmological parameters, *Astronomy & Astrophysics* **641**, A6 (2020).

[42] P. Gregory, *Bayesian Logical Data Analysis for the Physical Sciences: A Comparative Approach with Mathematica® Support* (Cambridge University Press, 2005).

[43] C. M. Bishop and N. M. Nasrabadi, *Pattern recognition and machine learning*, Vol. 4 (Springer, 2006).

[44] R. B. Nelsen, *An introduction to copulas* (Springer, 2006).

[45] Y. Chen and M. U. Gutmann, Adaptive gaussian copula abc, in *The 22nd International Conference on Artificial Intelligence and Statistics* (PMLR, 2019) pp. 1584–1592.

[46] M. Sklar, Fonctions de répartition à  $n$  dimensions et leurs marges, in *Annales de l'ISUP*, Vol. 8 (1959) pp. 229–231.

[47] P. Kumaraswamy, A generalized probability density function for double-bounded random processes, *Journal of hydrology* **46**, 79 (1980).

[48] M. D. Hoffman, D. M. Blei, C. Wang, and J. Paisley, Stochastic variational inference, the *Journal of machine Learning research* **14**, 1303 (2013).

[49] D. M. Blei, A. Kucukelbir, and J. D. McAuliffe, Variational inference: A review for statisticians, *Journal of the American statistical Association* **112**, 859 (2017).

[50] L. Dinh, J. Sohl-Dickstein, and S. Bengio, Density estimation using real nvp, arXiv preprint arXiv:1605.08803 (2016).

[51] A. Paszke, S. Gross, F. Massa, A. Lerer, J. Bradbury, G. Chanan, T. Killeen, Z. Lin, N. Gimelshein, L. Antiga, *et al.*, Pytorch: An imperative style, high-performance deep learning library, *Advances in neural information processing systems* **32** (2019).

[52] E. Bingham, J. P. Chen, M. Jankowiak, F. Obermeyer, N. Pradhan, T. Karaletsos, R. Singh, P. Szerlip, P. Horsfall, and N. D. Goodman, Pyro: Deep universal probabilistic programming, *Journal of machine learning research* **20**, 1 (2019).

[53] G. J. Székely and M. L. Rizzo, Energy statistics: A class of statistics based on distances, *Journal of statistical planning and inference* **143**, 1249 (2013).

[54] J. Weaver, I. Davidzon, S. Toft, O. Ilbert, H. McCracken, K. Gould, C. Jespersen, C. Steinhardt, C. Lagos, P. Capak, *et al.*, Cosmos2020: The galaxy stellar mass function—the assembly and star formation cessation of galaxies at  $0.2 < z < 7.5$ , *Astronomy & Astrophysics* **677**, A184 (2023).

[55] I. Davidzon, O. Ilbert, C. Laigle, J. Coupon, H. McCracken, I. Delvecchio, D. Masters, P. Capak, B. Hsieh, O. Le Fèvre, *et al.*, The cosmos2015 galaxy stellar mass function—thirteen billion years of stellar mass assembly in ten snapshots, *Astronomy & astrophysics* **605**, A70 (2017).

[56] V. Rodriguez-Gomez, S. Genel, M. Vogelsberger, D. Sijacki, A. Pillepich, L. V. Sales, P. Torrey, G. Snyder, D. Nelson, V. Springel, *et al.*, The merger rate of galaxies in the *Illustris* simulation: a comparison with observations and semi-empirical models, *Monthly Notices of the Royal Astronomical Society* **449**, 49 (2015).

[57] O. Fakhouri, C.-P. Ma, and M. Boylan-Kolchin, The merger rates and mass assembly histories of dark matter haloes in the two millennium simulations, *Monthly Notices of the Royal Astronomical Society* **406**, 2267 (2010).

[58] C. Lacey and S. Cole, Merger rates in hierarchical models of galaxy formation, *Monthly Notices of the Royal Astronomical Society* **262**, 627 (1993).

[59] V. Springel *et al.*, Simulations of the formation, evolution and clustering of galaxies and quasars, *Nature* **435**, 629 (2005).

[60] J. Kormendy and L. C. Ho, Coevolution (or not) of supermassive black holes and host galaxies, *Annual Review of Astronomy and Astrophysics* **51**, 511–653 (2013).

[61] A. E. Reines and M. Volonteri, Relations between central black hole mass and total galaxy stellar mass in the local universe, *The Astrophysical Journal* **813**, 82 (2015).

[62] F. Pacucci and A. Loeb, The redshift evolution of the  $m \bullet m$  relation for jwst's supermassive black holes at  $z > 4$ , *The Astrophysical Journal* **964**, 154 (2024).

[63] M. Volonteri, The formation and evolution of massive black holes, *Science* **337**, 544–547 (2012).

[64] V. Langen, N. Tamanini, S. Marsat, and E. Bortolas, Hierarchical bayesian inference on an analytical toy model of the lisa mbhb population (2025).

[65] P. Ajith, S. Babak, Y. Chen, M. Hewitson, B. Krishnan, J. Whelan, B. Bruegmann, P. Diener, J. Gonzalez, M. Hannam, *et al.*, A phenomenological template family for black-hole coalescence waveforms, *Classical and Quantum Gravity* **24**, S689 (2007).

[66] P. Ajith, M. Hannam, S. Husa, Y. Chen, B. Brügmann, N. Dorband, D. Müller, F. Ohme, D. Pollney, C. Reisswig, *et al.*, Inspiral-merger-ringdown waveforms for black-hole binaries with nonprecessing spins, *Physical Review Letters* **106**, 241101 (2011).

[67] T. Robson, N. J. Cornish, and C. Liu, The construction and use of lisa sensitivity curves, *Classical and Quantum Gravity* **36**, 105011 (2019).

[68] N. Cornish and T. Robson, Galactic binary science with the new lisa design, in *Journal of Physics: Conference Series*, Vol. 840 (IOP Publishing, 2017) p. 012024.

[69] A. Klein, E. Barausse, A. Sesana, A. Petiteau, E. Berti, S. Babak, J. Gair, S. Aoudia, I. Hinder, F. Ohme, *et al.*, Science with the space-based interferometer elisa: Supermassive black hole binaries, *Physical Review D* **93**, 024003 (2016).

[70] S. Khan and R. Green, Gravitational-wave surrogate models powered by artificial neural networks, *Physical Review D* **103**, 064015 (2021).

[71] C. Cutler and E. E. Flanagan, Gravitational waves from merging compact binaries: How accurately can one extract the binary's parameters from the inspiral waveform?, *Physical Review D* **49**, 2658 (1994).

[72] M. Vallisneri, Use and abuse of the fisher information matrix in the assessment of gravitational-wave parameter-estimation prospects, *Physical Review D—Particles, Fields, Gravitation, and Cosmology* **77**, 042001 (2008).

[73] T. B. Littenberg and N. J. Cornish, Prototype global analysis of lisa data with multiple source types, *Physical Review D* **107**, 063004 (2023).

[74] R. Srinivasan, E. Barausse, N. Korsakova, and R. Trotta, Simulation-based population inference of lisa's galactic binaries: Bypassing the global fit (2025).

[75] M. Fishbach, D. E. Holz, and B. Farr, Are ligo's black holes made from smaller black holes?, *The Astrophysical Journal Letters* **840**, L24 (2017).

[76] H. Gabbard, M. Williams, F. Hayes, and C. Messenger, Matching matched filtering with deep networks for gravitational-wave astronomy, *Physical review letters* **120**, 141103 (2018).

[77] M. Volonteri, F. Haardt, and P. Madau, The assembly and merging history of supermassive black holes in hierarchical models of galaxy formation, *The Astrophysical Journal* **582**, 559–573 (2003).

[78] P. Madau and M. J. Rees, Massive black holes as population iii remnants, *The Astrophysical Journal* **551**, L27–L30 (2001).

[79] G. Lodato and P. Natarajan, Supermassive black hole formation during the assembly of pre-galactic discs, *Monthly Notices of the Royal Astronomical Society* **371**, 1813–1823 (2006).

[80] A. Sesana, J. Gair, E. Berti, and M. Volonteri, Reconstructing the massive black hole cosmic history

through gravitational waves, *Physical Review D* **83**, 10.1103/physrevd.83.044036 (2011).

[81] E. Barausse, J. Bellovary, E. Berti, K. Holley-Bockelmann, B. Farris, B. Sathyaprakash, and A. Sesana, Massive black hole science with elisa, *Journal of Physics: Conference Series* **610**, 012001 (2015).

[82] C. L. Rodriguez, P. Amaro-Seoane, S. Chatterjee, K. Kremer, F. A. Rasio, J. Samsing, C. S. Ye, and M. Zevin, Post-newtonian dynamics in dense star clusters: Formation, masses, and merger rates of highly-eccentric black hole binaries, *Phys. Rev. D* **98**, 123005 (2018).

[83] D. Gerosa and M. Fishbach, Hierarchical mergers of stellar-mass black holes and their gravitational-wave signatures, *Nature Astronomy* **5**, 749–760 (2021).

[84] R. Essick, A. Farah, S. Galauadage, C. Talbot, M. Fishbach, E. Thrane, and D. E. Holz, Probing extremal gravitational-wave events with coarse-grained likelihoods, *The Astrophysical Journal* **926**, 34 (2022).